

# Crystal defects in monocrystalline silicon induced by spot laser melting

Cite as: J. Appl. Phys. **127**, 093102 (2020); doi: [10.1063/1.5142676](https://doi.org/10.1063/1.5142676)

Submitted: 16 December 2019 · Accepted: 14 February 2020 ·

Published Online: 2 March 2020



View Online



Export Citation



CrossMark

T. Menold,<sup>1,a)</sup> E. Hadjixenophontos,<sup>2</sup> R. Lawitzki,<sup>2</sup> G. Schmitz,<sup>2</sup> and M. Ametowobla<sup>1</sup>

## AFFILIATIONS

<sup>1</sup> Robert Bosch GmbH, Corporate Sector Research, 71272 Renningen, Germany

<sup>2</sup> Institute for Materials Science, University of Stuttgart, Heisenbergstrasse 3, 70569 Stuttgart, Germany

<sup>a)</sup>Author to whom correspondence should be addressed: [Tobias.Joachim.Menold@de.bosch.com](mailto:Tobias.Joachim.Menold@de.bosch.com)

## ABSTRACT

Laser processing of monocrystalline silicon has become an important tool for a wide range of applications. Here, we use microsecond spot laser melting as a model experiment to investigate the generation of crystal defects and residual stress. Using Micro-Raman spectroscopy, defect etching, and transmission electron microscopy, we find no dislocations in the recrystallized volume for cooling rates exceeding  $|dT/dt| = 2 \times 10^7$  K/s, and the samples remain free of residual stress. For cooling rates less than  $|dT/dt| = 2 \times 10^7$  K/s, however, the experiments show a sharp transition to a defective microstructure that is rich in dislocations and residual stress. Moreover, transmission electron microscopy indicates dislocation loops, stacking-fault tetrahedra, and voids within the recrystallized volume, thereby indicating supersaturation of intrinsic point defects during recrystallization. Complementing photoluminescence spectroscopy indicates even three regimes with decreasing cooling rate. Spectra of regime 1 do not contain any defect related spectral lines. In regime 2, spectral lines appear related to point defect clusters. In regime 3, the spectral lines related to point defect clusters vanish, but dislocation-related ones appear. We propose a quantitative model explaining the transition from dislocation-free to dislocation-rich recrystallization by means of the interaction between intrinsic point defects and dislocations.

Published under license by AIP Publishing. <https://doi.org/10.1063/1.5142676>

## I. INTRODUCTION

Laser processing of silicon recently became interesting in a wide range of applications. Typical applications are in the fields of microelectronics and micromechanics,<sup>1</sup> photovoltaics,<sup>2</sup> microfluidics,<sup>3</sup> bio- and nanotechnologies,<sup>4</sup> and microphotonics.<sup>5</sup>

Relevant laser processes, for example, laser doping, melt parts of silicon.<sup>6,7</sup> Unfortunately, there are experimental conditions in which the recrystallized volume after laser melting and final freezing contains dislocation (DI)s and other undesired crystal defects.<sup>8–15</sup> These crystal defects are especially harmful if the global thermal impact allows no subsequent annealing steps, for instance, in micromechanics.<sup>16</sup>

Presently, there exists no fundamental investigation on the relevant process parameter discriminating whether laser melting induces dislocations or not. Furthermore, the mechanism how laser melting leads to dislocation formation in an initially dislocation-free substrate remains unclear. Is it solely the thermal stress combined with plastic deformation or does supersaturation of point defects lead to condensation and nucleation of dislocation segments, similar to (particle) irradiation or quenching experiments?

The present contribution investigates spot laser melting as a model process and shows, that there is a threshold laser pulse energy  $E_p^{th}$  depending on the laser pulse length  $\tau_p$  and the focal diameter  $d_f$ . Below this threshold, the recrystallized volume contains no dislocations and remains free of residual stress. For  $E_p > E_p^{th}$ , however, the recrystallized microstructure becomes rich in dislocations and residual stress. For a pulse length of  $\tau_p = 115\ \mu s$  and a spot width of  $d_f = 65\ \mu m$ , the critical threshold is concretely found at  $E_p^{th} = 8.8\ mJ$ . Additionally, photoluminescence spectroscopy (PLS) and transmission electron microscopy (TEM) give evidence of intrinsic point defect supersaturation that developed during recrystallization and cooling.

TEM identifies dislocation loops, stacking-fault tetrahedra, and voids. PLS furthermore divides the laser processed structures into three regimes. In the order of increasing pulse energy, regime 1 does not contain defect related spectral lines. The dominant spectral lines in regime 2 are related to clusters of intrinsic point defects. Finally, dislocation-related spectral lines become dominant in regime 3.

A numerical simulation computes the cooling for the laser parameters of regimes 1–3 and demonstrates that the cooling rates

decrease with increasing laser pulse energy. So, the laser parameters of regime 1 lead to significant faster cooling than those of regimes 2 and 3. The threshold cooling rate for the transition from dislocation-free to dislocation-rich recrystallization (for regimes 2–3) is predicted at  $|dT/dt|_{th} \approx 2 \times 10^7 \text{ K/s}$ . An analytical model explains the formation of different microstructure by the absorption of excess point defects to dislocation segments and yields the sharp transition in agreement to the experiment.

## II. EXPERIMENTAL SETUP AND METHODS

The laser system used is the TruFiber 500 fiber laser (TRUMPF GmbH + Co. KG), the specifications of which are listed in **Table I**. An objective lens with a focal length  $f = 255 \text{ mm}$  focuses the Gaussian-shaped laser beam to a focal diameter  $d_f = 65 \mu\text{m}$ . Typical pulse lengths  $\tau_p$  and pulse energies  $E_p$  are  $30 \mu\text{s} \leq \tau_p \leq 1 \text{ ms}$  and  $1 \text{ mJ} \leq E_p \leq 100 \text{ mJ}$ , respectively. Such a laser pulse melts a diameter of a few tens of micrometers on a  $\{100\}$ -oriented monocrystalline silicon substrate of thickness  $d_s = 525 \mu\text{m}$ . The boron-doped Czochralski (CZ) grown substrates have an electrical resistivity  $\rho_{el} = (10 \pm 5) \Omega\text{cm}$ . During the laser processing, the substrates stay at room temperature within a vacuum chamber at an ambient pressure of  $p = 100 \text{ Pa}$  to prevent pore formation.<sup>17</sup>

To analyze the produced crystal defects, we perform micro-Raman spectroscopy,<sup>18,19</sup> selective defect etching,<sup>20</sup> transmission electron microscopy (TEM),<sup>21</sup> and photoluminescence spectroscopy (PLS).<sup>22</sup> The spatially resolved micro-Raman spectroscopy uses a helium-neon laser for excitation. The optical penetration depth  $\delta_p$  of the  $\lambda = 633 \text{ nm}$  excitation is  $\delta_p \approx 3 \mu\text{m}$ .<sup>23</sup> A microscope objective lens focuses the excitation light to  $3 \mu\text{m}$  width and additionally collects the scattered light that carries the relevant information. The spacing between measured points is also  $3 \mu\text{m}$ . An optical grating with grating parameter  $g = 1800 \text{ mm}^{-1}$  divides the scattered light spectrally. In unstressed silicon, the Raman peak (Stokes peak) lies at a wave number  $v \approx 520 \text{ cm}^{-1}$  with respect to the Rayleigh peak.<sup>18</sup> Mechanical stress shifts the Raman peak: tensile stress shifts to smaller wave number while compressive stress shifts to higher wave number. In addition, the linewidth of the Raman peak contains information about the crystal defect density. The reason why crystal defects broaden the Raman peak lies in the reduced phonon lifetimes.<sup>19</sup> Thus, we also analyzed the full width at half maximum *FWHM* of the Raman peak. The micro-Raman spectroscopy is performed both from the top view and in cross section. The cross sections are prepared using metallographic grinding and polishing; the final polishing step uses a

polishing suspension with 60 nm granulation. The cross section orientation is parallel to a  $\{110\}$  plane.

Additionally, standard defect etching according to Secco etches some of the cross sections.<sup>20</sup> Subsequently, a confocal laser scanning microscope visualizes the etch pits if the sample contains dislocations.

A Philips CM200-FEG obtains the presented TEM micrographs. Therefore, a focused ion beam (FIB) prepares lamellae in a Dual-Beam microscope (FEI-Scios). The lamellae are parallel to a  $\{100\}$  or to a  $\{110\}$  lattice plane, which goes right through the symmetry axis of the laser-melted structure.

The PLS uses  $\lambda = 532 \text{ nm}$  frequency-doubled Nd:YAG laser (Laser 2000) radiation for excitation. During the measurements, the samples are kept in a cryostat at liquid-helium temperature  $T = 4.2 \text{ K}$ .

In addition to these experimental methods, we investigate the temperature fields resulting from laser melting by means of a numerical model. The details of the model and its experimental validation are discussed in a previous contribution.<sup>24</sup>

## III. RESULTS

**Figure 1** presents light-optical micrograph in (a) top view and (b) in cross section for structures created by a  $\tau_p = 1 \text{ ms}$  laser pulse with a pulse energy of  $E_p = 72.4 \text{ mJ}$ . **Figures 1(c)** and **1(d)** show comparable micrographs for  $\tau_p = 35 \mu\text{s}$  and  $E_p = 4.8 \text{ mJ}$ . Remarkably, the shorter, less energetic laser pulse melts nearly the same radius as the previous. This first unexpected behavior is due to a strongly temperature-dependent optical absorption at the processing wavelength  $\lambda = 1070 \text{ nm}$ . The shorter laser pulse has a higher optical intensity and so heats the material faster to higher temperatures. In combination with the strongly temperature-increasing absorption coefficient,<sup>25</sup> this leads to a higher deposited energy rate in a kind of self-amplifying process.

**Figures 1(e), 1(f)** and **1(g), 1(h)** show mappings of the Raman peak shifts with respect to the unprocessed reference for the long and the short laser pulse, respectively. The mappings in **Figs. 1(e)** and **1(f)** present shifts ranging from  $\Delta v = -0.6 \text{ cm}^{-1}$  to  $\Delta v = 0.4 \text{ cm}^{-1}$  and so indicate residual stress within the recrystallized volume for the long laser pulse. The negative shifts indicate tensile stress in the  $\langle 011 \rangle$  direction, and the positive shifts compressive stress in the  $\langle 010 \rangle$  direction. In contrast to the long laser pulse, the short pulse produces no significant residual stress.

Furthermore, the long laser pulse obviously generates significant crystal defects as the linewidth of the Raman peak increases by as much as  $\Delta FWHM = 40\%$  compared to the non-exposed reference. **Figures 1(i)** and **1(j)** show the spatial distribution of the linewidth broadening from the top view and in cross section, respectively, for the long laser pulse. **Figures 1(k)** and **1(l)** show the same for the short laser pulse. As with the residual stress, the shorter laser pulse produces significantly fewer crystal defects than the longer one.

However, micro-Raman spectroscopy is not able to specify the types of crystal defects in detail. Therefore, we analyze the crystal defects using TEM. **Figure 2(a)** shows a bright-field TEM micrograph of a lamella that is cut from a structure generated by the  $\tau_p = 1 \text{ ms}$ ,  $E_p = 72.4 \text{ mJ}$  laser pulse, while **Fig. 2(c)** shows the

**TABLE I.** Specifications of TruFiber 500 fiber laser (delivered by TRUMPF GmbH + Co. KG).

TruFiber 500	
Wavelength $\lambda$ (nm)	$1070 \pm 10$
Power $P_0$ (W)	15–500
Pulse length $\tau_p$ ( $\mu\text{s}$ )	$15\text{--}\infty$
Beam quality factor $M^2$	<1.1

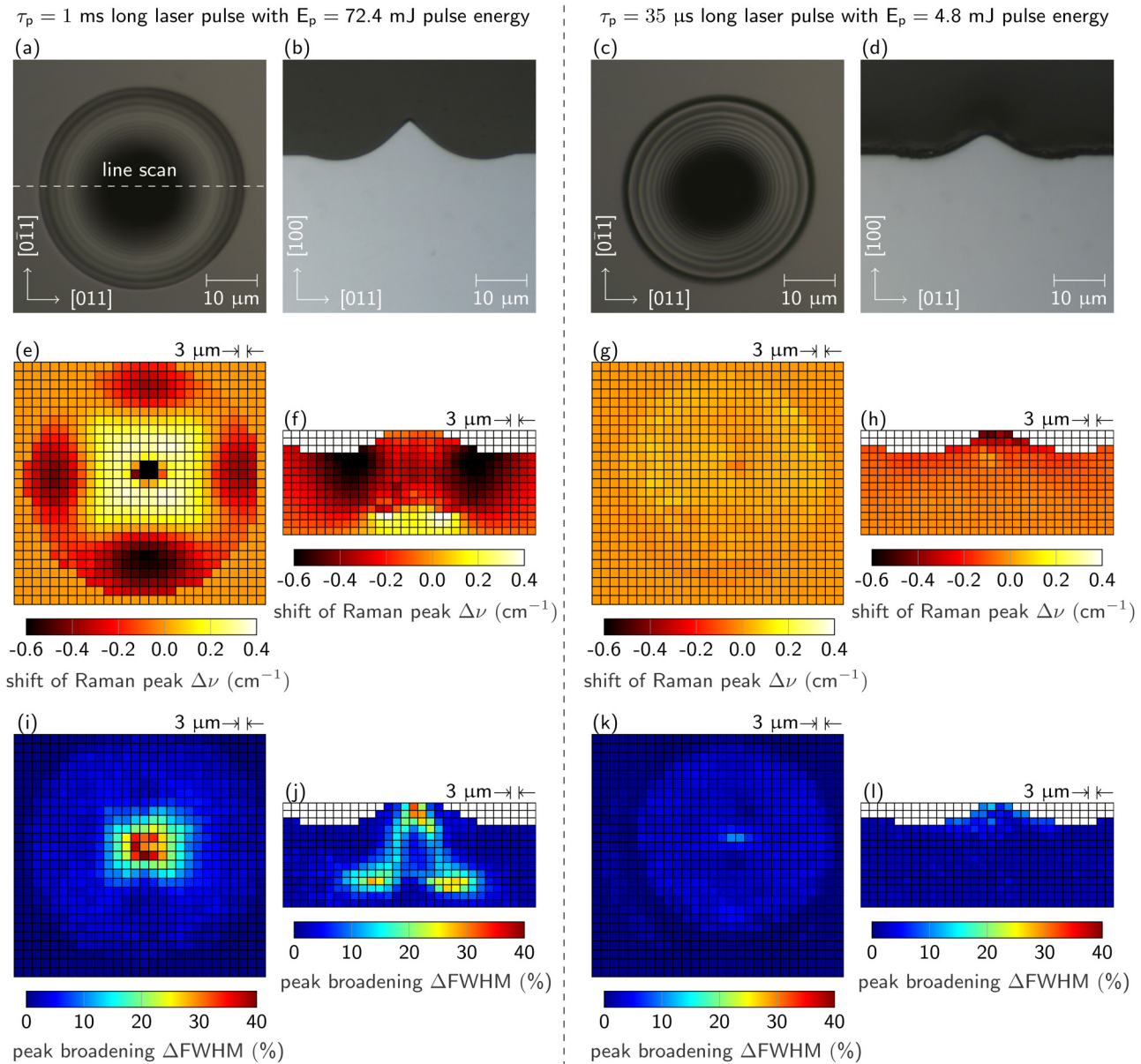


**FIG. 1.** Micro-Raman spectroscopy demonstrates that the choice of laser parameters discriminates between recrystallization free of or rich in residual stress. Residual stress shifts the Raman peak compared to an unstressed reference. Additionally, spectroscopy reveals that residual stress is correlated with crystal defects in the recrystallized volume since an increased defect density broadens the Raman peak compared to a defect-free reference. In the case of stress-free recrystallization, no significant increase of crystal defect density is measurable. Figures (a)–(d) show optical micrographs from top view and in cross section of structures created by a  $\tau_p = 1\text{ ms}$ ,  $E_p = 72.4\text{ mJ}$  laser pulse and a  $\tau_p = 35\text{ }\mu\text{s}$ ,  $E_p = 4.8\text{ mJ}$  one. The corresponding measurements of Raman peak shift and broadening are shown in (e)–(h) and (i)–(l), respectively.

same for a structure generated by the  $\tau_p = 35\text{ }\mu\text{s}$ ,  $E_p = 4.8\text{ mJ}$  laser pulse. Both lamellae are viewed along a  $\langle 100 \rangle$ -zone axis. The insets in Figs. 2(b) and 2(d) show the respective diffraction patterns, both of which indicate perfect epitaxial recrystallization.

However, in the case of the long pulse, the bright-field image in Fig. 2(a) contains a high density of crystal defects, of which the majority are dislocations (DIs). Additionally, stacking faults (SFs) appear and small clusters (CLs) that are arranged in rows. In

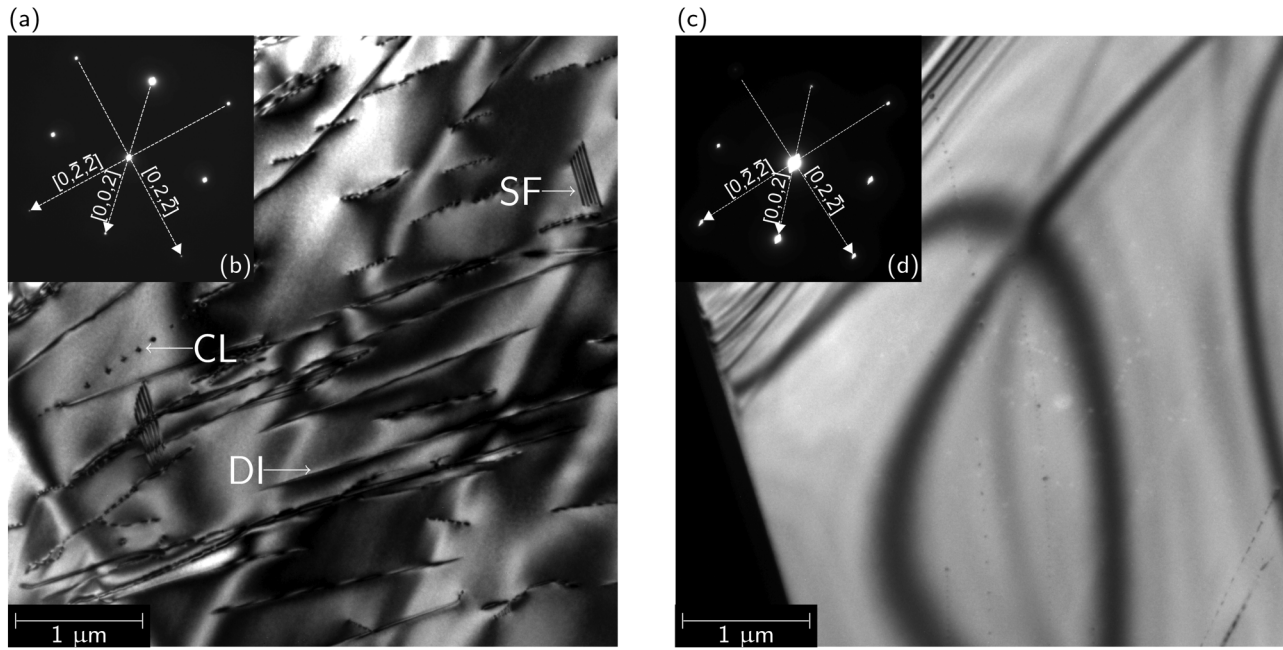


**FIG. 2.** Transmission electron microscopy (TEM) of recrystallized volumes after a long laser pulse ( $\tau_p = 1 \text{ ms}$ ,  $E_p = 72.4 \text{ mJ}$ ) (a) and a short laser pulse ( $\tau_p = 35 \mu\text{s}$ ,  $E_p = 4.8 \text{ mJ}$ ) (b). The long laser pulse induced a high density of dislocations (DI), stacking faults (SFs), and small clusters (CLs). By contrast, the comparable volume obtained after a short laser pulse appears practically defect-free (except bending contours). The corresponding diffraction patterns in (b) and (d) demonstrate perfect epitaxial recrystallization.

clear contrast, the structure generated by the short laser pulse in Fig. 2(c) shows a significantly lower defect density. The volume does not contain any dislocations or stacking faults, and the remaining clusters are smaller than in the previous example. Indeed, Fig. 2(c) shows the only region of the lamella in which we could find any crystal defects. The position is close to the top of the structure induced by spot laser melting.

Besides the impact of the laser pulse length at approximately constant radius of the melt pool, we also investigated the impact of the laser pulse energy  $E_p$  or power  $P = E_p/\tau_p$  at constant laser pulse length. In order to save measuring time, micro-Raman spectroscopy is restricted to line scans. The dashed line in the map of Fig. 1(a) indicates direction and position of these scans. They follow the  $\langle 011 \rangle$  axis and go through the center of the laser-affected zone. To quantify the strain energy, we estimate the local uniaxial stress along the scanning line from the peak shift  $\Delta\nu$  of the Raman signal (see Refs. 18 and 19),

$$\sigma = \xi \Delta\nu, \quad \xi = -500 \text{ MPa cm}. \quad (1)$$

Taking the square of the stress and integrating over the line-scan volume, a relative measure for the total strain energy is obtained

$$E_s = \frac{1}{2E} \int_{V_l} \sigma^2 dV, \quad (2)$$

where  $E \approx 169 \text{ GPa}$  is Young's modulus in the  $\langle 011 \rangle$  direction.<sup>26</sup> The integral in Eq. (2) covers the complete line-scan volume  $V_l$ , and the volume element is  $dV \approx (3 \mu\text{m})^3$  because of the excitation laser's focus diameter  $d_f = 3 \mu\text{m}$ , and the  $3 \mu\text{m}$  deep optical penetration depth.

Figure 3(a) shows  $E_s$  within the line-scan volume for structures induced by  $\tau_p = 1 \text{ ms}$ ,  $\tau_p = 115 \mu\text{s}$  and  $\tau_p = 35 \mu\text{s}$  laser pulses in dependence on the pulse power. For  $\tau_p = 1 \text{ ms}$  and  $\tau_p = 115 \mu\text{s}$ , there exists a clear threshold power  $P^{th}$  above which micro-Raman spectroscopy detects residual stress and thus considerable strain energy  $E_s > 0$ . The transition appears strikingly sharp. In the case of the  $\tau_p = 115 \mu\text{s}$  laser pulses, the corresponding threshold is marked at  $P^{th} = 76.6 \text{ W}$ , or  $E_p^{th} = P^{th} \tau_p = 8.8 \text{ mJ}$ . For  $\tau_p = 35 \mu\text{s}$ , micro-Raman spectroscopy does not measure residual stress in the case of  $P \leq 137 \text{ W}$ . For  $P > 137 \text{ W}$ , evaporation significantly deforms the surface of the structure, making it difficult to compare with an exclusively melting process.

Using Secco defect etching, we investigated the transition from residual stress-free to residual stress-rich recrystallization with another independent method. Figures 4(a)–4(f) show cross sections of spot laser-melting-induced structures with  $\tau_p = 115 \mu\text{s}$  laser pulses, where the Secco etching shows etch pits if the sample contains dislocations.

For a laser pulse power of  $P \leq 76.6 \text{ W}$ , the etched cross sections do not contain any etch pits. For  $P \geq 80.5 \text{ W}$ , the Secco etching visualizes dense dislocations in the cross sections. Obviously, the transition from residual stress-free to residual stress-rich recrystallization

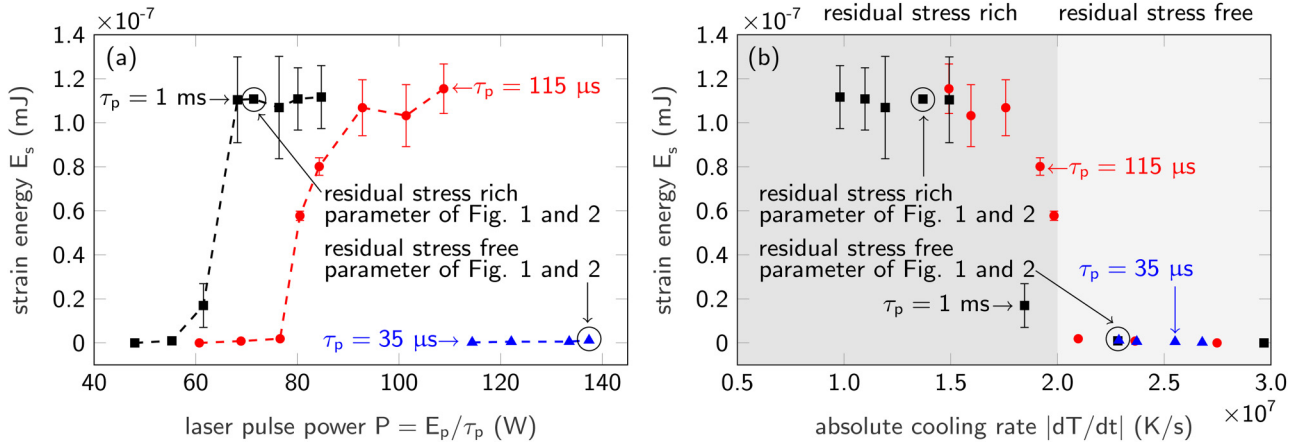


**FIG. 3.** Elastic strain energy as derived from the peak shift of the micro-Raman signal according to Eqs. (1) and (2) plot vs laser power (a) and cooling rate (b). Different symbols mark results for different pulse lengths:  $\tau_p = 1\text{ ms}$  (squares),  $\tau_p = 115\mu\text{s}$  (circles), and  $\tau_p = 35\mu\text{s}$  (triangles). For  $\tau_p = 1\text{ ms}$  and  $\tau_p = 115\mu\text{s}$ , a clear threshold laser pulse power  $P^{th} = E_p^{th}/\tau_p$  is identified above which micro-Raman spectroscopy reveals significant residual mechanical stress.<sup>17</sup> For  $\tau_p = 35\mu\text{s}$ , no residual stress is measurable until evaporation significantly deforms the surface of the structure for  $P > 137\text{ W}$ . The cooling rates  $dT/dt$  of (b) are calculated from the laser parameters by means of a numerical model. Remarkably, data of different pulse lengths fall on an unique master curve when plotted vs the cooling rate.  $|dT/dt| = 2 \times 10^7\text{ K/s}$  is identified as a general critical threshold. Data for  $\tau_p = 1\text{ ms}$  and  $\tau_p = 115\mu\text{s}$  in (a) are reused with permission from Menold *et al.*, Proc. SPIE Laser Applications in Microelectronic and Optoelectronic Manufacturing (LAMOM), XXIV, 109050X (2019).

corresponds to a transition from dislocation-free to dislocation-rich recrystallization. Furthermore, the etch pit distribution [e.g., in Fig. 4(f)] strongly resembles the distribution of Raman peak broadening in Fig. 1(j), which suggests that the Raman peak broadening originates from dislocations. Indeed, the dislocations are the microscopic root cause of the residual stress.<sup>27</sup> The elastic far fields of the dislocations within the recrystallized volume superpose, yielding the macroscopic stress that the micro-Raman spectroscopy detects.

To find the relevant physical parameter that controls the appearance of dislocations, we compute time-dependent temperature fields for the different laser parameters. Evaluating the temperature at the bottom of the melt pool [where the recrystallization begins at time  $t = 0$ , as marked in Fig. 4(b)] yields cooling curves for the corresponding laser parameter. The computed laser powers are calibrated to reproduce the experimentally measured melt pool radius  $R_{melt}$ . Figure 5(a) exemplifies cooling curves for pulses of  $\tau_p = 1\text{ ms}$  at different pulse powers  $P = E_p/\tau_p$ . A higher laser pulse energy melts a greater volume and thus the releasing latent heat of solidification causes a slower recrystallization,<sup>24</sup> and slower cooling of the recrystallized material. Fitting the cooling curves by straight lines [dashed in Fig. 5(a)] yields the initial cooling rates  $dT/dt$ , which Fig. 5(b) presents for  $\tau_p = 35\mu\text{s}$ ,  $\tau_p = 115\mu\text{s}$ , and  $\tau_p = 1\text{ ms}$  laser pulses at different laser pulse powers  $P$ . The clear correlation between laser power and cooling rates allows transforming the pulse powers in Fig. 3(a) into the corresponding cooling rates  $|dT/dt|$ , which yields the curves in Fig. 3(b). By this, we discover that, independent of  $\tau_p$ , the produced strain energy  $E_s$ , rises abruptly if  $|dT/dt|$  falls below the threshold value  $|dT/dt|_{th} \approx 2 \times 10^7\text{ K/s}$ .

In order to clarify the mechanism for the transition from dislocation-free to dislocation-rich recrystallization, we investigate the clusters of Figs. 2(a) and 2(c) in detail. Figure 6 shows

a detailed analysis of a region with high cluster density. Energy-dispersive x-ray spectroscopy (EDX) in the cluster region of Fig. 6 gives no hint of impurity precipitates. However, some of the clusters in Fig. 6 resemble small dislocation loops. The experimental finding of dislocation loops indicates interstitial supersaturation, because the nucleation barrier for vacancy-type dislocation loops is higher than the one for voids.<sup>28</sup> Thus, excess interstitials *inter alia* condensate to dislocation loops whereas excess vacancies form voids. Additionally, Fig. 6 identifies pinned dislocations, whereby the distance between the pinning points is  $d_{pin} \approx 50\text{ nm}$ . The obstacles, which pin the dislocation are sessile dislocation segments. For instance, Fig. 7 shows a HRTEM micrograph of a cluster in a structure generated by a  $\tau_p = 115\mu\text{s}$  laser pulse with  $E_p = 9.3\text{ mJ}$ , whereby the zone axis is parallel to the  $\langle 110 \rangle$  direction. The cluster resemble a stacking-fault tetrahedron,<sup>27</sup> and the structure of the stacking-fault tetrahedron is similar to the one found by Coene *et al.* in ion-implanted silicon after thermal annealing.<sup>29</sup> The condensation of stacking-fault tetrahedra is possible from excess interstitials as well as from excess vacancies.<sup>29</sup>

Additionally to pure interstitial-type clusters, we also find pure vacancy-type aggregates. Figures 8(a) and 8(b) show a part of the same lamella, originating from the dislocation-free structure generated by a  $\tau_p = 35\mu\text{s}$ ,  $E_p = 4.8\text{ mJ}$  laser pulse. However, the image in (b) was recorded 10 months after the image in (a). Both images identify some of the observed clusters as voids, but comparing Figs. 8(a) and 8(b) indicates that the voids continue to grow despite the fact that the lamella remained at room temperature. In contrast, a similar comparison of two figures of the microstructure produced by a  $\tau_p = 1\text{ ms}$ ,  $E_p = 72.4\text{ mJ}$  laser pulse, which contains dislocations, reveals no further evolution of remaining voids, even after 10 months of room temperature aging.

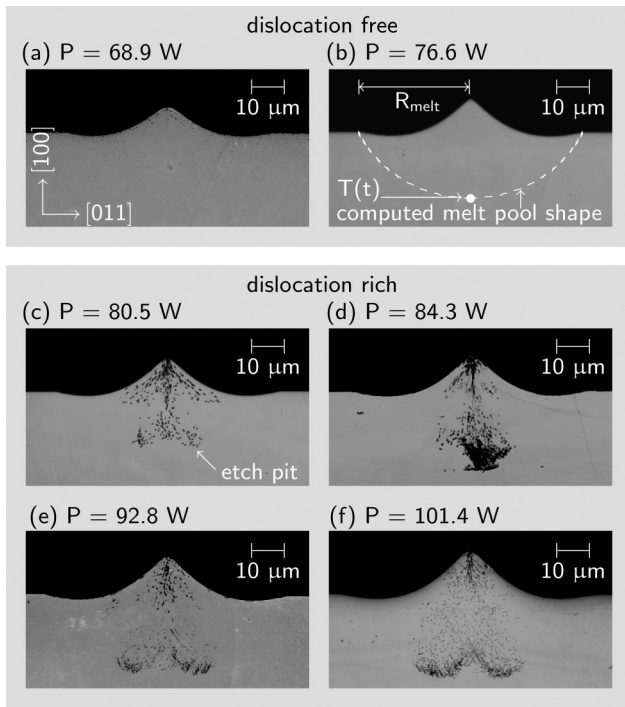


**FIG. 4.** Secco defect etching of cross sections through the laser-exposed zones produced by  $\tau_p = 115\mu\text{s}$  laser pulses. The pulse powers are  $P = 68.9\text{ W}$  in (a),  $P = 76.6\text{ W}$  in (b),  $P = 80.5\text{ W}$  in (c),  $P = 84.3\text{ W}$  in (d),  $P = 92.8\text{ W}$  in (e), and  $P = 101.4\text{ W}$  in (f). The etching identifies the dislocations as dark pits. Obviously, formation of the dislocations requires at least a critical power of  $P = 80.5\text{ W}$ . Mind the geometric similarity between the dislocation rich zones and the regions of Raman peak broadening in Fig. 1(j).

Besides TEM, PLS appeared as a suitable method to characterize defects related to point defect supersaturation. Other authors have used PLS, e.g., to investigate point defect supersaturation related defects in silicon stemming from irradiation or implantation.<sup>22,30</sup> Therefore, we also perform PLS on structures induced by spot laser melting. The irradiated structures are arranged in an array with  $20\mu\text{m}$  spacing between the laser-affected zones. The inset in Fig. 9(a) exemplifies an array of structures generated by  $\tau_p = 115\mu\text{s}$  laser pulses with  $E_p = 10.7\text{ mJ}$ . A dashed circle marks the size of the PLS measuring spot, which amounts to  $d_f = (400 \pm 100)\mu\text{m}$  and so overlaps several of the laser-generated structures.

The PL spectra in Figs. 9(a)–9(d) divide the laser-generated structures into three regimes. Figure 9(a) shows a regime 1 spectrum of structures generated by  $\tau_p = 35\mu\text{s}$  and  $E_p = 2.4\text{ mJ}$  laser pulses, producing  $|dT/dt| = 7.80 \times 10^7\text{ K/s}$ . The regime 1 spectrum exhibits no significant defect related spectral line.

Figures 9(b) and 9(c) visualize regime 2 spectra. The spectrum in Fig. 9(b) stems from structures generated by  $\tau_p = 115\mu\text{s}$  and  $E_p = 7.9\text{ mJ}$  laser pulses, and the spectrum in Fig. 9(c) is derived from  $\tau_p = 1\text{ ms}$  and  $E_p = 56.1\text{ mJ}$  structures. With  $|dT/dt| = 2.32 \times 10^7\text{ K/s}$  and  $|dT/dt| = 2.19 \times 10^7\text{ K/s}$  do both

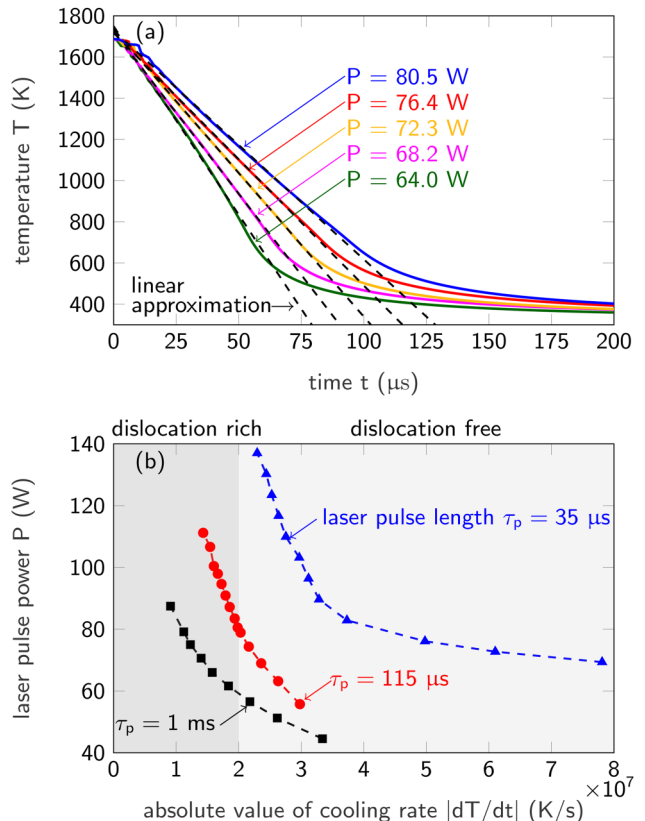


**FIG. 5.** Numerical calculation of the temperature at the bottom of the melt pool after exposure. Figure 4(b) sketches the point where  $T(t)$  is evaluated. The example curves in (a) show the cooling after  $\tau_p = 1\text{ ms}$  laser pulse exposure. Approximating the cooling curves in the high-temperature regime ( $T > 0.5T_m$ ) linearly, as (a) exemplifies, yields the correlation between the laser parameter and the initial cooling rate, as shown in (b).

pulses not produce dislocations but are close to the transition to dislocation-rich crystallization. Regime 2 spectra exhibit significant spectral lines that typically appear for ion-implanted samples after annealing. Table II gives the detailed values of the measured defect-correlated spectral lines and compares them with literature values. Dominant is the W line at  $E_{ph} = 1.012\text{ eV}$  that Bürger *et al.* found after He implantation.<sup>30</sup> Using molecular dynamics simulations, other authors identified the luminescence center of the W line as an interstitial cluster containing three self-interstitial atoms.<sup>31–33</sup> Responsible for the interstitial clustering is a supersaturated interstitial concentration.

By contrast, in the case of a dislocation rich microstructure for regime 3, the radiation-damage-correlated spectral lines decrease or vanish but dislocation-correlated spectral lines appear. Figure 9(d) shows a regime 3 spectrum taken from structures generated by  $\tau_p = 115\mu\text{s}$  and  $E_p = 10.7\text{ mJ}$  laser pulses, producing  $|dT/dt| = 1.65 \times 10^7\text{ K/s}$ . Dominant is the D1 line at  $E_{ph} = 0.827\text{ eV}$ , which Drozdov *et al.* and Sauer *et al.*<sup>34,35</sup> related to dislocations. The D1 line in Fig. 9(b) is strongly broadened and

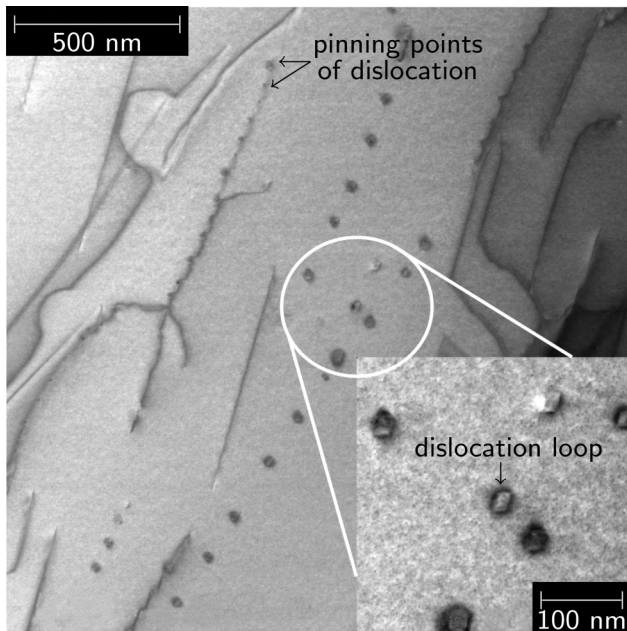


**FIG. 6.** TEM in higher resolution identifies some of the clusters as dislocation loops. The dislocation loops form because of the aggregation of interstitials. Additionally, the micrograph shows dislocations which are pinned to obstacles (e.g., sessile dislocation segments). EDX in the cluster and dislocation regions gives no hints of impurity precipitates.

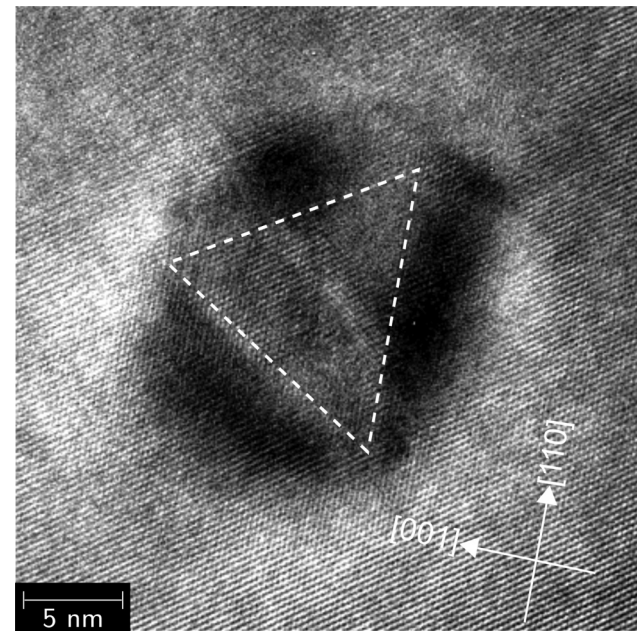


**FIG. 7.** High-resolution TEM (HRTEM) provides evidence that some clusters (as shown in Fig. 2) are stacking-fault tetrahedra. They develop from the condensation of intrinsic point defects and indicate supersaturation of intrinsic point defects in the recrystallizing volume.

shows a shift compared to the literature value of  $E_{ph} = 0.807$  eV, which indicates a rather high dislocation density.<sup>35</sup>

#### IV. DISCUSSION

The PL spectra and the extended point defect cluster observed by microscopy indicate that crystallization after spot laser melting

leads to supersaturation of intrinsic point defects. In the following, we discuss our experimental findings in the context of supersaturated intrinsic point defects. We first show that the typical recrystallization velocities produce a clear point defect supersaturation and estimate the expected concentrations. Finally, we introduce an analytical model that explains the transition from dislocation-free to dislocation-rich recrystallization by the absorption of point defects by the dislocations.

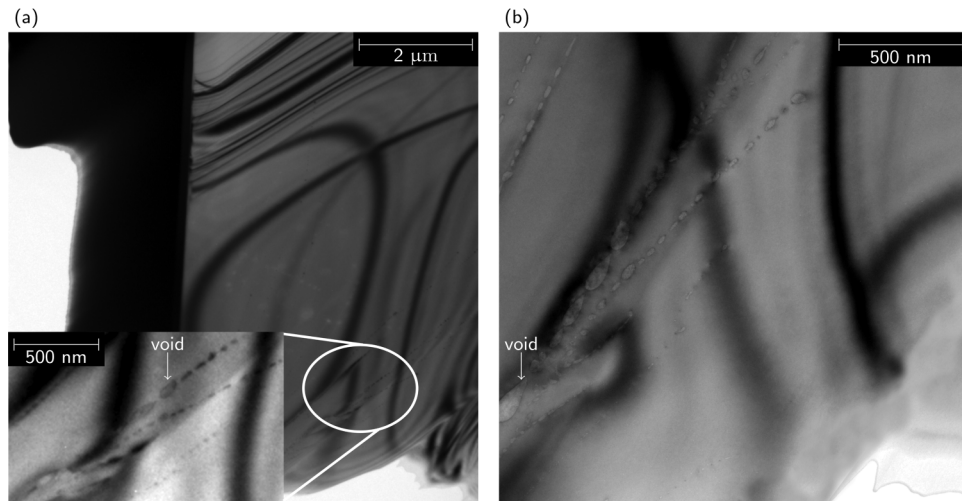


**FIG. 8.** Besides interstitial-type cluster, TEM identifies vacancy-type ones as well, like voids in the dislocation-free structure generated by a  $\tau_p = 35\ \mu s$ ,  $E_p = 4.8\ mJ$  laser pulse. The TEM images in (a) and (b) stem from the same lamella, but the image in (b) was recorded 10 months after the image in (a) and shows that the voids continue to grow even at room temperature. In dislocation rich samples, we observe no change in the microstructure with time because the dislocations absorb the excess point defects (not shown).

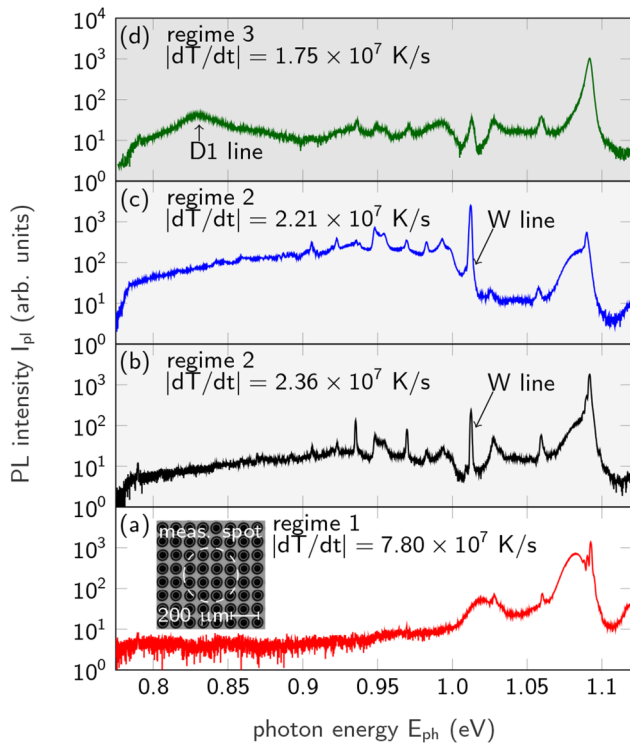


**FIG. 9.** Photoluminescence spectroscopy (PLS) divides the laser-generated structures into three regimes. The regime 1 spectrum in (a) from structures generated by  $\tau_p = 35\mu s$  and  $E_p = 2.4\text{ mJ}$  laser pulses exhibits no defect related spectral line. The regime 2 spectra in (b) and (c) from structures generated by  $\tau_p = 115\mu s$  and  $E_p = 7.9\text{ mJ}$  laser pulses in (b), or by  $\tau_p = 1\text{ ms}$  and  $E_p = 56.1\text{ mJ}$  laser pulses in (c) show spectral lines that typically exist in irradiated or implanted samples after annealing. Dominant is the W line, whose luminescence center is a cluster of self-interstitial atoms. When the laser parameters produce dislocations as with  $\tau_p = 115\mu s$ ,  $E_p = 10.7\text{ mJ}$  in (d), regime 3 spectra are obtained. For regime 3 spectra, the W line decreases or vanishes but dislocation-related spectral lines such as D1 line appears.

**TABLE II.** Defect-correlated spectral lines in the photoluminescence spectra of Figs. 9(a)–9(d).

Measured photon energy $E_{ph}$ (meV)	Literature value $E_{ph}$ (meV)	Interpretation
1059	1060	Radiation damage at 100 K <sup>22</sup>
1027	1025	Electron irradiation damage <sup>22</sup>
1012	1012	W line, but found due to He implantation, <sup>22,30</sup> the luminescence is from an interstitial cluster <sup>31–33</sup>
993 (strongly broadened)	997	Dislocation-related center (D4 line) <sup>22,34,35</sup>
993	$990 \pm 10$	Ion implantation damage and hydrogenation <sup>22</sup>
969.7	969.5	G line <sup>22</sup>
954.2	953.9	Perturbed from G line <sup>22</sup>
948.2	947	Radiation damage and 450 °C annealing <sup>22</sup>
935.3	935.1	Radiation damage involving C and 450 °C annealing <sup>22</sup>
922.9	922.3	High-temperature annealing <sup>22</sup>
827 (strongly broadened)	807	Dislocation-related tetragonal center (D1 line) <sup>22,34,35</sup>

### A. Supersaturation of intrinsic point defects during recrystallization

During recrystallization, when the crystallization front moves with the velocity  $v_{re}$ , the vacancy and interstitial concentration  $c_v$ ,  $c_i$  satisfy in one-dimensional approximation,<sup>36,37</sup>

$$\frac{\partial c_v}{\partial t} = \frac{\partial}{\partial x} \left( D_v \frac{\partial c_v}{\partial x} \right) - v_{re} \frac{\partial c_v}{\partial x} - k_{iv} (c_v c_i - c_v^{eq} c_i^{eq}), \quad (3)$$

$$\frac{\partial c_i}{\partial t} = \frac{\partial}{\partial x} \left( D_i \frac{\partial c_i}{\partial x} \right) - v_{re} \frac{\partial c_i}{\partial x} - k_{iv} (c_v c_i - c_v^{eq} c_i^{eq}). \quad (4)$$

The diffusion coefficients  $D_{v,i}$ , the equilibrium concentrations  $c_{v,i}^{eq}$ , and the vacancy interstitial recombination rate  $k_{iv}$  are strongly dependent on the temperature  $T$ . The Appendix summarizes the material parameters that we use herein. The equilibrium concentrations show a dependence on the external and internal stresses as well.<sup>38</sup> The first term on the right-hand side of Eqs. (3) and (4) represents diffusive transport, the second the advection due to the moving crystallization front, and the third the recombination of a vacancy-type and an interstitial-type point defect due to Frenkel's reaction.<sup>36,37</sup> The coordinate system is chosen so that the crystallization front stays at  $x = 0$  while the crystal moves in the positive  $x$  direction,

In a previous work, we showed that recrystallization velocities for spot laser melting under comparable experimental conditions amount to  $10\text{ cm/s} < v_{re} < 1000\text{ cm/s}$ .<sup>24</sup> In this range of  $v_{re}$ , the advection term dominates Eqs. (3) and (4). Therefore, the equations decouple and simplify to

$$\frac{\partial c_k}{\partial t} = -v_{re} \frac{\partial c_k}{\partial x}, \quad k = v, i. \quad (5)$$

For the boundary conditions, we assume constant point defect concentrations on the crystallization front, which depend on the recrystallization velocity  $v_{re}$ , namely,

$$c_k(t)|_{x=0} = c_k^\circ(v_{re}), \quad k = v, i. \quad (6)$$

For  $v_{re} \rightarrow 0$ , the point defect concentrations on the crystallization front are equal to melting point's equilibrium concentrations  $c_{v,i}^{\circ}(v_{re} = 0) = c_{v,i}^{eq}(T_m)$  due to Schottky's reaction.<sup>36</sup> However, as Webb and Bolling *et al.* pointed out,<sup>39,40</sup> fast crystallization from the melt may cause entrapment of point defects, thereby exceeding melting point's equilibrium concentrations  $c_{v,i}^{\circ}(v_{re}) > c_{v,i}^{eq}(T_m)$ .

Originally, Webb and Bolling *et al.* investigated the entrapment of vacancies during the crystallization of metals, which is caused by the fact that liquid metals are less dense as the crystals.<sup>39,40</sup> Liquid silicon however is more dense as the crystal. This density anomaly is actually the reason for the peaklike structure that spot laser melting produces and which Figs. 1(a)–1(d) exemplify.<sup>24</sup> Thus, for the rapid recrystallization after laser melting, we assume a more pronounced entrapment of interstitials. Considering the well-known Voronkov criterion, the assumption of a more pronounced interstitial entrapment initially appears to be contra intuitive.<sup>41</sup> Voronkov showed, that if the ratio of crystallization velocity over the temperature gradient near the crystallization front exceeds a critical value, the crystal is rich in vacancies; otherwise, more interstitials are present.<sup>41</sup> However, Voronkov derived his criterion focusing on typical pulling rates for crystal growth processes according to the Czochralski or floating zone technique. For that pulling rates, which are orders of magnitude slower than the recrystallization velocity after laser melting no point defect entrapment takes place and the complete coupled equations in (3) and (4) together with  $c_{v,i}^{\circ} = c_{v,i}^{eq}(T_m)$  yield the Voronkov criterion.<sup>41</sup>

The interstitial rich recrystallization after laser melting, we observe furthermore experimentally in regime 2 PL spectra. The luminescence center of the dominant W line is an interstitial cluster containing three self-interstitial atoms,<sup>31–33</sup> which forms in order to decrease interstitial supersaturation. Following the concept of Webb and Bolling *et al.*, we may calculate the interstitial entrapment by<sup>39,40</sup>

$$c_i^{\circ}(v_{re}) = c_i^{eq}(T_m) + \frac{(\rho_l^{at} - \rho_s^{at}) - c_i^{eq}(T_m)}{1 + \frac{D_l(T_m)}{v_{re} a_{Si}}}. \quad (7)$$

Here,  $\rho_{ls}^{at}$  are the atomic densities in the liquid and the solid phase and  $a_{Si} = 5.431 \text{ \AA}$  is silicon's lattice parameter.<sup>42</sup> Using  $\rho_l^{at} - \rho_s^{at} \approx 3 \times 10^{21} \text{ cm}^{-3}$  yields  $10^{18} \text{ cm}^{-3} < c_i^{\circ}(v_{re}) < 10^{20} \text{ cm}^{-3}$ .

Besides the boundary condition on the melt-solid-interface at  $x = 0$ , we have to consider the condition for  $\lim_{x \rightarrow \infty} c_{v,i}$  as well as an initial condition  $c_{v,i}(t = 0)$ . For  $x \rightarrow \infty$ , the temperature remains at the base temperature  $T = T_0$ , so

$$\lim_{x \rightarrow \infty} c_k = c_k^{eq}(T_0), \quad k = v, i. \quad (8)$$

Comparing  $c_{v,i}^{\circ} \geq c_{v,i}^{eq}(T_m)$  with  $c_{v,i}^{eq}(T_0)$  for  $T_0 = 300 \text{ K}$  justifies the approximation  $c_{v,i}^{eq}(T_0) \approx 0$ . Furthermore, neglecting diffusion's impact, we approximate the initial point defect distribution by

$$c_{v,i}(x)|_{t=0} = c_{v,i}^{\circ}(v_{re}) \Theta(-x), \quad x \geq 0, \quad (9)$$

whereby  $\Theta$  denotes the Heaviside step function.

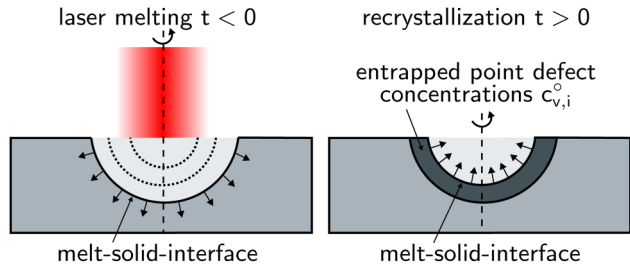


**FIG. 10.** The fast recrystallization after laser melting causes point defect entrapment and thereby supersaturated concentrations of of intrinsic point defects within the recrystallized volume.

The solution of Eq. (5) considering the boundary conditions in Eqs. (6) and (8) and the initial condition in Eq. (9) is

$$c_{v,i}(x, t) = c_{v,i}^{\circ}(v_{re}) \Theta(-(x - v_{re}t)), \quad x \geq 0. \quad (10)$$

This solution simply describes a situation in which  $c_{v,i}^{\circ}(v_{re}) \geq c_{v,i}^{eq}(T_m)$  freezes into the recrystallized region  $0 < x < v_{re}t$ . However, our previous work showed, that in spot laser melting under comparable experimental conditions, the temperature  $T$  decreases with  $\eta \sim 10^8 \text{ K/m}$ ,<sup>24</sup> leading to a supersaturation of intrinsic point defects in the recrystallized volume. Figure 10 sketches the considered scenario for the melt pool geometry of a single laser pulse. As a consequence of the supersaturation, the chemical potential  $\mu_{v,i}$  for the respective point defect species,

$$\mu_{v,i} = k_B T \log\left(\frac{c_{v,i}}{c_{v,i}^{eq}}\right), \quad (11)$$

is greater than zero, indicating non-equilibrium conditions.<sup>27</sup>

To decrease supersaturation, the excess point defects form clusters.<sup>43</sup> In silicon, the vacancy-type point defects form voids, and the interstitials follow a clustering cascade over {311} defects to dislocation loops.<sup>36,43–46</sup> The condensation of stacking-fault tetrahedra is possible for vacancies as well as for interstitials.<sup>43</sup> Condensed or nucleated dislocation segments reduce supersaturation further by absorbing point defects. Thereby, a dislocation segment moves by climbing. Triggered by climbing, the dislocation density may increase further by multiplication if the dislocations are pinned to obstacles like voids, stacking-fault tetrahedra, or sessile dislocation loops. However, all the possible processes are diffusion limited and thus depend strongly on temperature. As a consequence, the cooling rate determines if and to what extent the supersaturation is reduced.

## B. Cooling rate as the dominant parameter

According to Fig. 5(b) the  $\tau_p = 35 \mu\text{s}$ ,  $E_p = 2.4 \text{ mJ}$  laser pulse of PLS regime 1 cools with  $|dT/dt| \approx 7.80 \times 10^7 \text{ K/s}$ . The fast cooling prevents the formation of clusters, which could act as optical centers visible in the PL spectrum.

If the cooling rate decreases like  $|dT/dt| = 2.30 \times 10^7 \text{ K/s}$  for the  $\tau_p = 35 \mu\text{s}$ ,  $E_p = 4.8 \text{ mJ}$  laser pulse, or  $|dT/dt| = 2.36 \times 10^7 \text{ K/s}$  for the  $\tau_p = 115 \mu\text{s}$ ,  $E_p = 7.9 \text{ mJ}$  laser pulse, the point defects are mobile long enough to form extended clusters, which we observe in regime 2 PL spectra. The luminescence center of the dominant W line in the regime 2 PL spectra of Figs. 9(b) and 9(c) is an interstitial cluster containing three self-interstitial atoms.<sup>31–33</sup> Additionally also vacancy-type aggregates like the voids in the TEM images of the  $\tau_p = 35 \mu\text{s}$ ,  $E_p = 4.8 \text{ mJ}$  structure in Figs. 8(a) and 8(b) are observable.

A further decrease in the cooling rate leads to a recrystallization that is rich in dislocations and residual stress. Figure 3(b) identifies  $|dT/dt|_{th} \approx 2 \times 10^7 \text{ K/s}$  as the threshold cooling rate. For structures induced by  $\tau_p = 1 \text{ ms}$ ,  $E_p = 72.4 \text{ mJ}$  laser pulses, the cooling rate is  $|dT/dt| = 1.33 \times 10^7 \text{ K/s}$  and the corresponding TEM image in Fig. 2(a) shows a variety of dislocations. Structures produced by  $\tau_p = 115 \mu\text{s}$ ,  $E_p = 9.3 \text{ mJ}$  cool with  $|dT/dt| = 1.98 \times 10^7 \text{ K/s} < |dT/dt|_{th}$  and the Secco defect etching in Fig. 4(c) visualize a high density of dislocations within the recrystallized volume. Additionally, micro-Raman spectroscopy in Fig. 3(a) measures residual stress for  $\tau_p = 115 \mu\text{s}$ ,  $E_p = 9.3 \text{ mJ}$ . In contrast,  $\tau_p = 115 \mu\text{s}$ ,  $E_p = 8.8 \text{ mJ}$  yields  $|dT/dt| = 2.09 \times 10^7 \text{ K/s} > |dT/dt|_{th}$  and the Secco defect etching in Fig. 4(b) visualize a dislocation-free recrystallized volume. Furthermore, micro-Raman spectroscopy in Fig. 3(a) does not measure residual stress. Next, we explain the transition from dislocation-free to dislocation-rich recrystallization at  $|dT/dt|_{th} \approx 2 \times 10^7 \text{ K/s}$  by means of point defect absorption to dislocation segments.

### C. Modeling the transition from dislocation-free to dislocation-rich recrystallization after laser melting

In the following, we consider solely interstitials, since we assume a more pronounced interstitial entrapment during recrystallization. The additional free energy because of interstitial supersaturation leads to condensation or nucleation of dislocation segments.<sup>27,47</sup> Subsequently, the dislocation nuclei may grow due to dislocation multiplication triggered by dislocation pinning and dislocation movement (gliding or climbing).<sup>27</sup> Dislocation climbing results from the absorption of interstitials, which further reduces their supersaturation. We assume a small nucleus dislocation density and derive a condition at which cooling rate the dislocation density grows by climbing and multiplication.

For the production rate of a climbing dislocation source, Wolfer and Glasgow proposed<sup>48</sup>

$$\frac{d}{dt}\rho = Kv_{cl}\rho. \quad (12)$$

Here,  $\rho$  denotes the dislocation density,  $v_{cl}$  is the average climbing velocity of dislocation segments, and  $K$  is a multiplication constant. Wolfer and Glasgow showed that  $K = 1/d_{pin}$  is the reciprocal of the distance  $d_{pin}$  between two pinning points that pin the dislocation segments.<sup>48</sup> From Fig. 6, we extract  $d_{pin} \approx 50 \text{ nm}$  and thus  $K \approx 2 \times 10^5 \text{ cm}^{-1}$ .

The number of excess interstitials  $dN$ , which a dislocation segment  $dl$  absorbs within the time interval  $dt$  is

$$dN = \pi(c_i - c_i^{eq})D_i dt dl \approx \pi D_i c_i dt dl, \quad (13)$$

yielding  $v_{cl}$  by<sup>27</sup>

$$v_{cl} = \frac{\Omega}{b} \frac{dN}{dt dl} = \pi \frac{\Omega}{b} D_i c_i. \quad (14)$$

Herein,  $b = 3.84 \times 10^{-8} \text{ cm}$  denotes the Burgers vector absolute value and  $\Omega = 2 \times 10^{-23} \text{ cm}^3$  the atomic volume.<sup>42</sup> The rate at which the interstitial concentration decreases is  $dc_i/dt = -dN/(dt dV)$ . With  $dV = (1/\rho) dl$  and Eq. (13), as well as inserting Eq. (14) into Eq. (12), our model consists of two coupled rate equations

$$\frac{d}{dt}c_i = -\pi D_i \rho c_i, \quad (15)$$

$$\frac{d}{dt}\rho = \frac{\pi K \Omega D_i}{b} \rho c_i. \quad (16)$$

The rate equations (15) and (16) are decouplable and analytically solvable using the invariant

$$\frac{K\Omega}{b} c_i + \rho = \text{const.}, \quad (17)$$

whereby the invariant is equal to the maximum dislocation density  $\rho_{max}$ , because in the limit  $c_i \rightarrow 0$  it is  $\rho = \rho_{max}$ . Thus, inserting  $\rho = \rho_{max} - (K\Omega/b) c_i$  in Eq. (15) decouples the rate equations for  $\rho$  and  $c_i$  and yields

$$\frac{d}{dt}c_i = -\pi D_i \left( \rho_{max} c_i - \frac{K\Omega}{b} c_i^2 \right). \quad (18)$$

Using separation of variables together with  $c_i(t=0) = c_i^\circ(v_{re})$  yields an analytical solution for  $c_i(t)$  and together with Eq. (17) also for  $\rho(t)$

$$\int_{c_i^\circ(v_{re})}^{c_i} \frac{dc}{\rho_{max} c - \frac{K\Omega}{b} c^2} = -\pi \int_0^t D(T(\tau)) d\tau = -\pi l_d^2(t), \quad (19)$$

$$c_i(t) = \frac{b\rho_{max}}{2K\Omega} \times \left\{ 1 - \tanh \left[ \frac{\pi\rho_{max}}{2} l_d^2(t) - \operatorname{artanh} \left( \frac{2K\Omega c_i^\circ(v_{re})}{b\rho_{max}} - 1 \right) \right] \right\}, \quad (20)$$

$$\rho(t) = \frac{\rho_{max}}{2} \times \left\{ 1 + \tanh \left[ \frac{\pi\rho_{max}}{2} l_d^2(t) - \operatorname{artanh} \left( \frac{2K\Omega c_i^\circ(v_{re})}{b\rho_{max}} - 1 \right) \right] \right\}. \quad (21)$$

Here,  $l_d^2(t) = \int_0^t D_i(T(\tau)) d\tau$  is the square of the diffusion length. Evaluating  $\rho$  and  $c_i$  at  $t_\infty$ , when the temperature  $T(t)$  reaches

approximately base temperature  $T_0$ , Eqs. (20) and (21) describe continuous step functions of  $\rho$  and  $c_i$  on the squared diffusion length  $l_d^2(t_\infty)$ . For a linear temperature decay, the squared diffusion length  $l_d^2(t_\infty)$  is inversely proportional to cooling rate  $l_d^2(t_\infty) = |\mathrm{d}T/\mathrm{d}t|^{-1} \int_{T_0}^{T_m} D_i(T) \mathrm{d}T$ . Hence, our model predicts consistently with the micro-Raman spectroscopy in Fig. 3(a) and the Secco defect etching in Fig. 4(a)–4(f), a rapid increase of dislocation density  $\rho$ , if the cooling rate  $|\mathrm{d}T/\mathrm{d}t|$  falls short of a threshold value

$$\left| \frac{\mathrm{d}T}{\mathrm{d}t} \right|_{th} = \frac{\pi \rho_{\max} \int_{T_0}^{T_m} D_i(T) \mathrm{d}T}{2 \operatorname{artanh} \left( \frac{2K\Omega c_i^\circ(v_{re})}{b\rho_{\max}} - 1 \right)}. \quad (22)$$

The TEM image in Fig. 2(a) yields  $\rho_{\max} \approx 10^9 \text{ cm}^{-2}$ . Thus, to achieve  $|\mathrm{d}T/\mathrm{d}t|_{th} = 2 \times 10^7 \text{ K/s}$ , the entrapped interstitial concentration has to satisfy

$$c_i^\circ(v_{re}) = \frac{b\rho_{\max}}{2K\Omega} \left[ \tanh \left( \frac{\pi \rho_{\max}}{2|\mathrm{d}T/\mathrm{d}t|_{th}} \int_{T_0}^{T_m} D_i(T) \mathrm{d}T \right) + 1 \right] \\ = 9.6 \times 10^{18} \text{ cm}^{-3}. \quad (23)$$

This entrapped interstitial concentration corresponds, regarding Eq. (7), to a recrystallization velocity of  $v_{re} \approx 24 \text{ cm/s}$ . For the  $\tau_p = 115 \mu\text{s}$ ,  $E_p = 9.3 \text{ mJ}$  laser pulse, which according to Fig. 4(c) is the minimal pulse energy that generates dislocations, our numerical model predicts an average axial recrystallization velocity  $v_{re} = 40.9 \text{ cm/s}$ , which is close to  $v_{re} \approx 24 \text{ cm/s}$ .

## V. CONCLUSION AND OUTLOOK

Using spot laser melting, we investigate the mechanisms for crystal defect formation in melting-regime laser processing of monocrystalline silicon. With the help of micro-Raman spectroscopy, Secco defect etching, and TEM, we find a transition from recrystallization that is free of dislocations and residual stress to one that is rich in them. Below a threshold laser pulse energy  $E_p^{th}$ , that depends on laser pulse length  $\tau_p$  (at a constant laser focus diameter), no dislocations are measurable and the sample remains free of residual stress. Above  $E_p^{th}$ , the laser process produces dislocations in the recrystallized volume leading to residual stress. A numerical model, that computes the temperature fields resulting from spot laser melting, relates the threshold laser parameter to a threshold cooling rate  $|\mathrm{d}T/\mathrm{d}t|_{th} = 2.0 \times 10^7 \text{ K/s}$ . For  $|\mathrm{d}T/\mathrm{d}t| > |\mathrm{d}T/\mathrm{d}t|_{th}$ , we observe a dislocation-free recrystallization. By contrast,  $|\mathrm{d}T/\mathrm{d}t| < |\mathrm{d}T/\mathrm{d}t|_{th}$  induces dislocation.

Additionally, HRTEM identifies dislocation loops, stacking-fault tetrahedra, and voids within the recrystallized volume. Furthermore, photoluminescence spectroscopy divides the laser molten structures into three regimes. Regime 1 does not contain defect related spectral lines. Regime 2 is characterized by spectral lines related to intrinsic point defect clusters. Dominant is the W line, whose luminescence center is a cluster containing three self-interstitial atoms. Spectra of regime 3 show dislocation-related spectral lines, with a dominant D1 line.

Considering these experimental findings, we conclude that during recrystallization after laser melting, intrinsic point defects are supersaturated. In order to minimize the free energy input stemming from the supersaturation, the point defects form clusters and subsequently dislocation segments nucleate or condensate. Assuming entrapment of interstitials on the melt-solid interface during recrystallization, due to silicon's density anomaly, we develop an analytical model. The model considers the increase of the dislocation density by climbing and multiplication. In agreement with our experimental findings, the model predicts a rapid growth of dislocation density if the cooling rate falls short of a threshold value.

The dislocation generation mechanism presented in this paper may be transferable to other melting regime laser processes, where it is not yet clear which mechanism generates the dislocations found, e.g., in nanosecond laser melting.<sup>10</sup> In contrast to spot laser melting with single shots of pulses, usual nanosecond laser processes use multiple pulses or scan the laser beam. In the case of multiple pulses with or without scanning, the overlapping laser pulses may strongly exceed the single pulse thermal impact and potentially generate dislocations by the same mechanism that the present contribution discusses.

For processes using ultra-short laser pulses, other authors report dislocation generation as well.<sup>49</sup> However, the generation mechanism differs from a melting-regime process. The ultra-short process induces a shock wave propagating into the bulk,<sup>50</sup> which causes dislocation generation.

## ACKNOWLEDGMENTS

The authors would like to thank J. H. Werner for working with us on the manuscript and K. Thonke for providing the photoluminescence spectra.

## APPENDIX: MATERIAL PROPERTIES

### 1. Diffusion coefficients:<sup>51</sup>

$$D_v(T) = 6.2614 \times 10^{-4} \text{ cm}^2/\text{s} \times \exp \left( \frac{-0.4 \text{ eV}}{k_B T} \right), \\ D_i(T) = 0.19497 \text{ cm}^2/\text{s} \times \exp \left( \frac{-0.9 \text{ eV}}{k_B T} \right).$$

### 2. Recombination coefficient:<sup>52</sup>

$$k_{iv}(T) = 1.2 \times 10^{-6} \text{ cm} [D_v(T) + D_i(T)] \\ \exp \left[ \frac{-0.58 \text{ eV} - k_B T (2.29 + 7.38 \times 10^{-3} \text{ K}^{-1} T)}{k_B T} \right].$$

### 3. Equilibrium concentrations:<sup>51</sup>

$$c_v^{eq}(T) = 7.59982 \times 10^{26} \text{ cm}^{-3} \times \exp \left( -\frac{4 \text{ eV}}{k_B T} \right), \\ c_i^{eq}(T) = 6.1859 \times 10^{26} \text{ cm}^{-3} \times \exp \left( -\frac{4 \text{ eV}}{k_B T} \right).$$

## REFERENCES

- <sup>1</sup>A. Dalili, B. Tan, and K. Venkatakrishnan, *Opt. Lasers Eng.* **48**, 346 (2010).
- <sup>2</sup>C. Dunsky, "Laser processes in PV manufacturing: An update," in *Industrial Laser Solutions* (2011), p. 26. Available at <http://www.industrial-lasers.com/articles/print/volume-26/issue-4/features/laser-processes-in-pv-manufacturing-an-update.html>
- <sup>3</sup>C. Priest, *Biomicrofluidics* **4**, 032206 (2010).
- <sup>4</sup>D. Rother, T. Sen, D. East, and I. J. Bruce, *Nanomedicine* **6**, 281 (2011).
- <sup>5</sup>T. Tsuchizawa, K. Yamada, H. Fukuda, T. Watanabe, J.-I. Takahashi, M. Takahashi, T. Shoji, E. Tamechika, S.-I. Itabashi, and H. Morita, *IEEE J. Sel. Top. Quantum Electron.* **11**, 232 (2005).
- <sup>6</sup>E. Fogarassy, R. Stuck, J. J. Grob, and P. Siffert, *J. Appl. Phys.* **52**, 1076 (1981).
- <sup>7</sup>T. Sameshima, S. Usui, and M. Sekiya, *J. Appl. Phys.* **62**, 711 (1987).
- <sup>8</sup>H. T. Nguyen, Y. Han, M. Ernst, A. Fell, E. Franklin, and D. Macdonald, *Appl. Phys. Lett.* **107**, 022101 (2015).
- <sup>9</sup>K. Ohmer, Y. Weng, J. R. Köhler, H. P. Strunk, and J. H. Werner, *IEEE J. Photovoltaics* **1**, 183 (2011).
- <sup>10</sup>Y. Weng, B. Kedjar, K. Ohmer, J. R. Köhler, J. H. Werner, and H. P. Strunk, *Phys. Status Solidi C* **10**, 28 (2013).
- <sup>11</sup>H. Baumgart, F. Phillipps, G. A. Rozgonyi, and U. Gösele, *Appl. Phys. Lett.* **38**, 95 (1981).
- <sup>12</sup>A. Cullis, H. C. Webber, N. G. Chew, J. M. Poate, and P. Baeri, *Phys. Rev. Lett.* **49**, 219 (1982).
- <sup>13</sup>M. Ametowbla, G. Bilger, J. R. Köhler, and J. H. Werner, *J. Appl. Phys.* **111**, 114515 (2012).
- <sup>14</sup>Z. Sun and M. C. Gupta, *Appl. Surf. Sci.* **456**, 342 (2018).
- <sup>15</sup>Z. Sun and M. C. Gupta, *J. Appl. Phys.* **124**, 223103 (2018).
- <sup>16</sup>K. E. Petersen, *Proc. IEEE* **70**, 420 (1982).
- <sup>17</sup>T. Menold, F. Lanoy, M. Ametowbla, S. Hinderberger, K. Ohmer, J. R. Köhler, and J. H. Werner, *Proc. SPIE XXIV*, 109050X (2019).
- <sup>18</sup>I. De Wolf, *Semicond. Sci. Technol.* **11**, 139 (1996).
- <sup>19</sup>G. Sarau, A. Bochmann, R. Lewandowska, and S. Christiansen, in *Advanced Aspects of Spectroscopy* (IntechOpen, London, 2012).
- <sup>20</sup>F. Secco, *J. Electrochem. Soc.* **119**, 948 (1972).
- <sup>21</sup>H. Kohl and L. Reimer, *Transmission Electron Microscopy: Physics of Image Formation* (Springer, Berlin, 2008).
- <sup>22</sup>G. Davies, *Phys. Rep.* **176**, 83 (1989).
- <sup>23</sup>M. A. Green and M. J. Keevers, *Prog. Photovoltaics Res. Appl.* **3**, 189 (1995).
- <sup>24</sup>T. Menold, M. Ametowbla, and J. R. Köhler, *J. Appl. Phys.* **124**, 163104 (2018).
- <sup>25</sup>G. E. Jellison, Jr. and D. H. Lowndes, *Appl. Phys. Lett.* **41**, 594 (1982).
- <sup>26</sup>A. Masolin, P.-O. Bouchard, R. Martini, and M. Bernacki, *J. Mater. Sci.* **48**, 979 (2013).
- <sup>27</sup>J. P. Hirth and J. Lothe, *Theory of Dislocations* (John Wiley & Sons, NJ, 1982).
- <sup>28</sup>T. Tan, P. Plekhanov, and U. M. Gösele, *Appl. Phys. Lett.* **70**, 1715 (1997).
- <sup>29</sup>W. Coene, H. Bender, and S. Amelinckx, *Philos. Mag. A* **52**, 369 (1985).
- <sup>30</sup>N. Bürger, K. Thonke, R. Sauer, and G. Pensl, *Phys. Rev. Lett.* **52**, 1645 (1984).
- <sup>31</sup>M. Aboy, I. Santos, P. López, L. A. Marqués, and L. Pelaz, *J. Electron. Mater.* **47**, 5045 (2018).
- <sup>32</sup>A. Carvalho, R. Jones, J. Coutinho, and P. Briddon, *Phys. Rev. B* **72**, 155208 (2005).
- <sup>33</sup>A. Mudryi, F. Korshunov, A. Patuk, I. Shakin, T. Larionova, A. Ulyashin, R. Job, W. Fahrner, V. Emel'yanov, V. Y. Davydov *et al.*, *Phys. B Condens. Matter* **308**, 181 (2001).
- <sup>34</sup>N. A. Drozdov, A. A. Patrin, and V. D. Tkachev, *Pisma Zh. Eksp. Teor. Fiz.* **23**, 651 (1976) [*JETP Lett.* **23**, 597 (1976)].
- <sup>35</sup>R. Sauer, J. Weber, J. Stolz, E. R. Weber, K.-H. Küsters, and H. Alexander, *Appl. Phys. A* **36**, 1 (1985).
- <sup>36</sup>S. M. Hu, *Mater. Sci. Eng. R Rep.* **13**, 105 (1994).
- <sup>37</sup>Y. Yoshida and G. Langouche, *Defects and Impurities in Silicon Materials* (Springer, Berlin, 2015).
- <sup>38</sup>K. Sueoka, E. Kamiyama, J. Vanhellemont, and K. Nakamura, *ECS Solid State Lett.* **3**, P69 (2014).
- <sup>39</sup>W. Webb, *J. Appl. Phys.* **33**, 1961 (1962).
- <sup>40</sup>G. Bolling and D. Fainstein, *Philos. Mag.* **25**, 45 (1972).
- <sup>41</sup>V. Voronkov, *J. Cryst. Growth* **59**, 625 (1982).
- <sup>42</sup>R. Hull, *Properties of Crystalline Silicon* (IET, Stevenage, 1999), Vol. 20.
- <sup>43</sup>H. Bernas, *Materials Science with Ion Beams* (Springer, Berlin, 2009), Vol. 116.
- <sup>44</sup>S. Coffa, S. Libertino, and C. Spinella, *Appl. Phys. Lett.* **76**, 321 (2000).
- <sup>45</sup>G. Pan, K. Tu, and S. Prussin, *Appl. Phys. Lett.* **71**, 659 (1997).
- <sup>46</sup>J. Li and K. S. Jones, *Appl. Phys. Lett.* **73**, 3748 (1998).
- <sup>47</sup>G. S. Was, *Fundamentals of Radiation Materials Science: Metals and Alloys* (Springer, Berlin, 2016).
- <sup>48</sup>W. Wolfer and B. Glasgow, *Acta Metall.* **33**, 1997 (1985).
- <sup>49</sup>J. Kaspar, A. Luft, S. Nolte, M. Will, and E. Beyer, *J. Laser Appl.* **18**, 85 (2006).
- <sup>50</sup>D. S. Ivanov and L. V. Zhigilei, *Phys. Rev. Lett.* **91**, 105701 (2003).
- <sup>51</sup>M. S. Kulkarni, V. Voronkov, and R. Falster, *J. Electrochem. Soc.* **151**, G663 (2004).
- <sup>52</sup>T. Sinno, R. A. Brown, W. von Ammon, and E. Dornberger, *J. Electrochem. Soc.* **145**, 302 (1998).